

Formation of asymmetric arms in barred galaxies

P. Sánchez-Martín,¹★ C. García-Gómez,² J. J. Masdemont³ and M. Romero-Gómez⁴

¹*IUMA, Universidad de Zaragoza, Dept. de Matemática Aplicada, Pedro Cerbuna, 12, 50009 Zaragoza, Spain*

²*D.E.I.M, Universitat Rovira i Virgili, Avd. Països Catalans, 26, 43007 Tarragona, Spain*

³*IEEC & Universitat Politècnica de Catalunya, Dept. de Matemàtiques, Diagonal 647, E08028 Barcelona, Spain*

⁴*Institut de Ciències del Cosmos (ICCUB), Universitat de Barcelona (IEEC-UB), Martí i Franquès 1, E08028 Barcelona, Spain*

Accepted 2023 January 21. Received 2023 January 19; in original form 2022 September 28

ABSTRACT

We establish a dynamical mechanism to explain the origin of the asymmetry between the arms observed in some barred disc galaxies, where one of the two arms emanating from the bar ends is very well defined, while the second one displays a ragged structure, extending between its ridge and the bar. To this purpose, we study the invariant manifolds associated with the Lyapunov periodic orbits around the unstable equilibrium points at the ends of the bar. Matter from the galaxy centre is transported along these manifolds to the periphery, forming this way the spiral arms that emanate from the bar ends. If the mass distribution in the galaxy centre is not homogeneous, because of an asymmetric bar with one side stronger than the other, or because of a non-centred bulge, the dynamics about the two unstable Lagrange points at the ends of the bar will not be symmetric as well. One of their invariant manifolds becomes more extended than the other, enclosing a smaller section and the escaping orbits on it are fewer and dispersed in a wider region. The result is a weaker arm and more ragged than the one at the other end of the bar.

Key words: galaxies: kinematics and dynamics – galaxies: structure – galaxies: spiral.

1 INTRODUCTION

A high fraction of disc galaxies appear to be barred (74 per cent to 85 per cent in automatic classifications or 36 per cent to 63 per cent with alternative methods (Lee, Ann & Park 2019)). These authors also suggest that strongly barred galaxies, classified as SBs, are preponderant in late-type galaxies. Most of these strongly barred galaxies appear to be asymmetric under a simple visual inspection. They usually present a strong bar and two spiral arms emanating from the bar ends, and frequently some inner rings as well. However, a detailed visual inspection of these galaxies, available in the STScI Digitized Sky Survey or in the Sloan Digital Sky Survey (SDSS) (Bundy et al. 2015), reveals that some barred galaxies exhibit important asymmetries in their spiral structure. While one of the two spiral arms is long and strongly defined, the second arm shows a ragged structure, and the matter is distributed irregularly between the ridge of the spiral arm and the bar. A non-symmetric distribution of matter in the galaxy disc can be a natural outcome, since disc galaxies may be formed through a combination of secular evolution and violent events, including smooth accretion, disc instabilities, and minor and major mergers (e.g. Tonini et al. 2016). In Fig. 1, we show some examples of galaxies showing asymmetric discs.

In this paper, we study the dynamic response of an asymmetric mass distribution on the orbital structure of barred galaxies, modelling the asymmetry of the central parts by a slightly off-centred bulge, which, viewing the galaxy as a whole, represents a simple but realistic model of an asymmetric bar. In this scenario, the Lagrange invariant points located at the bar ends will also

present an asymmetric orbital structure, as initially shown in Colin & Athanassoula (1989). The new step in this work is to additionally study the unstable periodic orbits around these Lagrange points and the associated unstable manifolds that provide escape routes for orbits which can transport material from the central regions to the outer parts of the discs (Romero-Gómez et al. 2006; Sánchez-Martín, Romero-Gómez & Masdemont 2016). These unstable manifolds are the backbones of the spiral arms emanating from the bar ends. In the case of asymmetric Lagrange points, however, the unstable manifolds also display important differences. The orbits following one of these manifolds are close together and can explain the presence of a strong spiral arm. On the other hand, the second manifold has a more open orbital structure, with its escaping orbits dispersed in a wider zone, causing the ragged structure of the second arm. Thus, the orbital structure of the unstable Lagrange points is able to explain the asymmetric phenomenology present in some of the strongly barred galaxies.

The paper is organized as follows: in Section 2, we quantify the level of asymmetry in asymmetric barred galaxies using a two-dimensional Fourier transform method. In Sections 3 and 4, we describe the asymmetric barred galaxy model used in this work and show the orbital analysis and invariant manifolds, respectively. Different approaches are summarized and conclusions are given in Section 5.

2 ANALYSIS OF THE BAR ASYMMETRY

In this paper, we model the galactic asymmetric mass distribution using a classical galactic model with three symmetric components (disc, bar, and bulge) but displacing slightly the bulge from the galaxy centre. This results in a total mass distribution biased towards

* E-mail: patricias@unizar.es

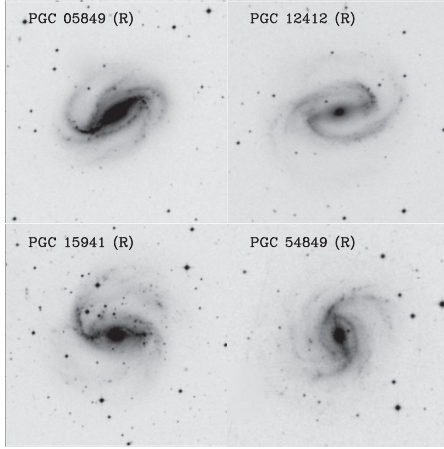


Figure 1. Images of some strongly barred galaxies showing the asymmetric spiral arm patterns in the R-filter from the STScI Digitized Sky Survey. In the top row, we show the galaxies PGC 05849 (NGC 0613) and PGC 12412 (NGC 1300) and in the bottom one PGC 15941 (NGC 1672) and PGC 54849 (NGC 5921).

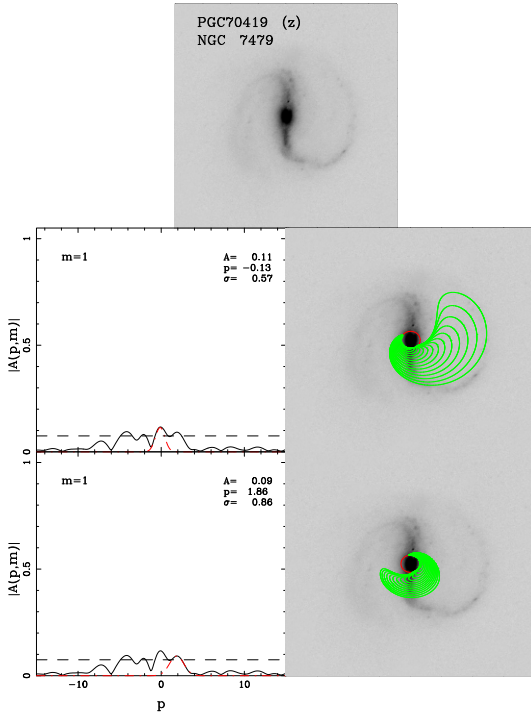


Figure 2. Analysis of the $m = 1$ component of the SDSS galaxy image of NGC 7479 in the z-filter. The upper panel shows the deprojected image of the galaxy. On the left of the middle and lower panels, we show the modulus of the $m = 1$ component of the Fourier spectrum, and with red-dashed lines two Gaussian components fitted to this modulus. In the respective right panels, we show in green the density distribution associated with each of these single components superimposed on the galaxy image.

one side of the bar. Many barred galaxies show some kind of asymmetries in their inner mass distribution with one side of the bar stronger than the other. An example is the galaxy NGC 1300, studied by Patsis, Kalapotharakos & Grosbol (2010). They generated a numerical model of the potential using K images of the galaxy. The resultant model was clearly asymmetric, containing a bar with a stronger arm. This model was used to study the orbits associated

with this asymmetric barred structure. Many barred galaxies show similar asymmetries. Some of these galaxies are shown in Fig. 1. In order to quantify these asymmetries, we can analyse in detail the mass distribution of one of the galaxies showing this phenomenology, namely the galaxy PGC 70419 (NGC 7479). For this purpose, we use a galaxy image from the SDSS survey in the infrared z-filter. Assuming a constant M/L ratio, the light distribution is a good tracer of the mass distribution in the disk. The image is previously cleaned from background stars and then deprojected using the FFT method (García-Gómez et al. 2004) giving a position angle (PA) of 38° and an inclination angle of 45° .

The image is then decomposed in its Fourier components using a technique first introduced by Considère & Athanassoula (1982), Iye et al. (1982), and further developed by García-Gómez et al. (2017). For deprojected image of the galaxy $I(u, \theta)$, where $u = \ln(r)$, we calculate the two-dimensional Fourier transform defined as

$$A(p, m) = \int_{u_{\min}}^{u_{\max}} \int_0^{2\pi} I(u, \theta) e^{i(pu + m\theta)} d\theta du, \quad (1)$$

where m is the azimuthal frequency, associated with the multiplicity of the structures, i.e. the number of arms while p is the radial frequency, associated with the pitch angle of the structure i , through the relation

$$p = -\frac{m}{\tan(i)}. \quad (2)$$

In this way, $m = 1$ spectrum contains the spiral components with no symmetry, $m = 2$ spectrum contains the components with a periodicity of π radians or bisymmetric signals, and so on for the rest of the m frequencies. Each of the azimuthal components $m = 1, 2, \dots$ can be further decomposed in its radial components using a Gaussian fit to the modulus and keeping the phase constant as follows:

$$|A(p, m)| = \sum_{j=1}^{N_g} C_j \exp -\frac{(p - p_j)^2}{2\sigma_j^2}. \quad (3)$$

In this relation, p_j represents the central frequency of the Gaussian, σ_j its dispersion, and C_j its amplitude. The number of Gaussians used in each fit, N_g , will depend on the complexity of the spectrum.

In the upper panel of Fig. 2, we show the deprojected SDSS galaxy image of NGC 7479 using the z-filter. Note that one of its arms is very pronounced, while the opposite arm appears diffuse. On the left of the middle and lower panels of this figure, we show the modulus of the Fourier spectrum of the $m = 1$ component which is associated with the asymmetries in the light distribution. The modulus of the Fourier components are normalized to the modulus of the stronger component, which in this case is $m = 2$ containing the bisymmetric signals of the strong bar and the spiral arms. The $m = 1$ spectrum shown here contains the spiral components responsible for the asymmetries in the mass distribution. The relative low values of the $m = 1$ in this scale shows that the mass asymmetry is a second-order effect for this galaxy. In red, we superpose two of the Gaussian components into which this signal is decomposed. These Gaussian components can be transformed back to obtain the density distribution associated with each particular spiral mode. The density distributions of these spiral components are presented in the respective right panels in green, superposed on the galaxy image. The isocontours come from the normalized density corresponding to the Gaussian components and show that the asymmetries are related to the southern end of the bar and the strong arm emanating from its end. This shows that the galaxy has an asymmetric mass distribution, biased to the southern part of the galaxy.

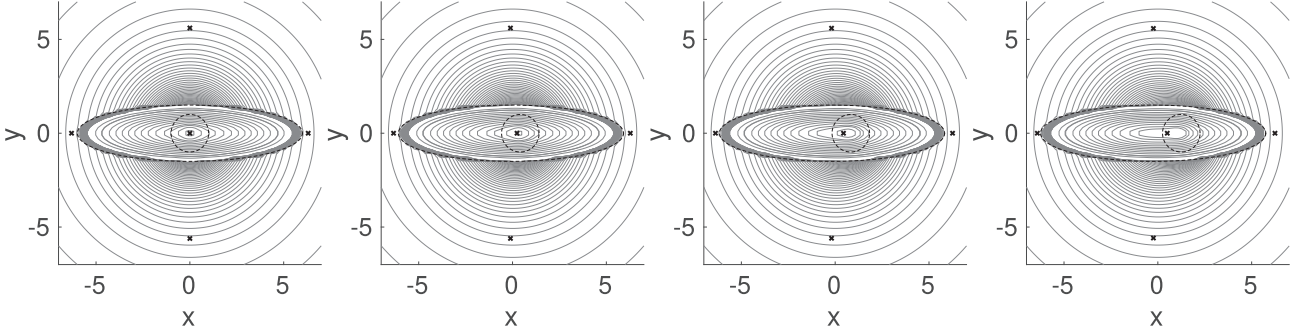


Figure 3. Isodensity curves of the potential $\phi = \phi_d + \phi_b + \phi_{bl}$. Equilibrium points of the system are marked with a cross. The Ferrers bar and the Plummer bulge are outlined by dotted black curves. From left to right: Bulge centred at (0,0,0), (0.5,0,0), (1,0,0), and (1.5,0,0).

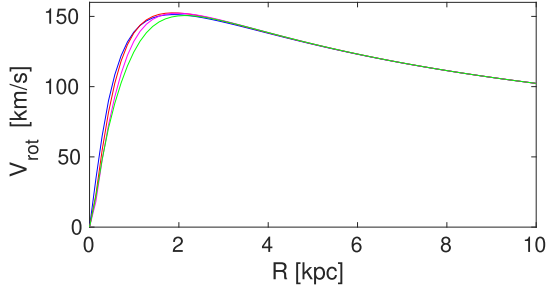


Figure 4. Rotation curve of the potential $\phi = \phi_d + \phi_b + \phi_{bl}$ for the bulge centred at (0,0,0) (in blue), (0.5,0,0) (in red), (1,0,0) (in magenta), and (1.5,0,0) (in green).

3 CHARACTERISTICS OF THE GALACTIC MODEL

The equations of motion of the classical galactic model (see e.g. Pfenniger 1984; Skokos, Patsis & Athanassoula 2002; Romero-Gómez et al. 2006; Sánchez-Martín et al. 2016) describe the movement of a particle in a gravitational potential ϕ . In the rotating frame, the equations of motion are described by

$$\ddot{\mathbf{r}} = -2(\Omega_p \times \dot{\mathbf{r}}) - \Omega_p \times (\Omega_p \times \mathbf{r}) - \nabla\phi, \quad (4)$$

where $\mathbf{r} = (x, y, z)$ is the position of the particle, ϕ is the total gravitational potential of the system, and Ω_p is the angular velocity of the bar around the z -axis, $\Omega_p = (0, 0, \Omega)$. The origin of the reference frame is located at the centre of mass of the system and the frame is aligned with the main axis of the bar.

The potential model ϕ used in this paper is a combination of three analytical components: an axisymmetric Miyamoto–Nagai disc with potential ϕ_d (Miyamoto & Nagai 1975), an ellipsoid Ferrers bar with potential ϕ_b (Ferrers 1877), and a bulge structure represented by a Plummer spheroid potential ϕ_{bl} (Plummer 1911). The total potential is the addition of these three components, $\phi = \phi_d + \phi_b + \phi_{bl}$.

The disc potential is described by the equation

$$\phi_d = -\frac{GM_d}{\sqrt{R^2 + (A + \sqrt{B^2 + z^2})^2}}, \quad (5)$$

where $R^2 = x^2 + y^2$ is the cylindrical coordinate radius of the potential in the disc plane and z is the vertical distance over the disc component. The parameters G , M_d , A , and B denote the gravitational constant, the disc mass, and the shape of the disc, respectively. Taking $A = 0$, the potential becomes the Plummer potential. The bar is modelled

by an ellipsoid with density function

$$\rho = \begin{cases} \rho_0 (1 - m^2)^{n_h}, & m \leq 1 \\ 0, & m > 1, \end{cases} \quad (6)$$

where $m^2 = x^2/a^2 + y^2/b^2 + z^2/c^2$, a (semi-major axis), b (intermediate axis), and c (semi-minor axis) determine the shape of the bar, n_h is the homogeneity degree of the mass distribution ($n_h = 2$ in our work), and ρ_0 is the density at the origin ($\rho_0 = \frac{105}{32\pi} \frac{GM_b}{abc}$ if $n_h = 2$, where M_b is the bar mass).

The unit of length considered is the kpc, the time unit is $u_t = 2 \times 10^6$ yr, Ω is in $[u_t]^{-1}$, and the mass unit is $u_M = 2 \times 10^{11} M_\odot$, where M_\odot denotes the mass of the Sun. G stands for the gravitational constant.

In our model, we select a disc radius of $A = 3$ kpc, height $B = 1$ kpc, and mass giving a value of $GM_d = 0.52 \text{ kpc}^3/u_t^2$. The dimensions of the bar are $a = 6$ kpc, $b = 1.5$ kpc, and $c = 0.4$ kpc, and its mass is such that $GM_b = 0.4 \text{ kpc}^3/u_t^2$. The Plummer bulge with a radius $B = 1$ kpc and GM_{bl} is set to have around 15 per cent of the mass of the bar GM_b , in order that $G(M_d + M_b + M_{bl}) = 1$. The bar pattern speed is fixed as $\Omega = 0.0633 [u_t]^{-1}$ ($\sim 30.97 \text{ km/s/kpc}$).

In the rotating reference frame aligned with the main axis of the bar, the equations of motion given in equation (4) are written as the following dynamical system:

$$\begin{cases} \ddot{x} = 2\Omega \dot{y} + \Omega^2 x - \phi_x \\ \ddot{y} = -2\Omega \dot{x} + \Omega^2 y - \phi_y \\ \ddot{z} = -\phi_z. \end{cases} \quad (7)$$

The Jacobi first integral of equation (4) (which can be regarded as the energy in the rotating frame) is given by

$$C_J(x, y, z, \dot{x}, \dot{y}, \dot{z}) = -(\dot{x}^2 + \dot{y}^2 + \dot{z}^2) + \Omega^2(x^2 + y^2) - 2\phi, \quad (8)$$

and the effective potential is defined by $\phi_{\text{eff}} = \phi - \frac{1}{2}\Omega^2(x^2 + y^2)$.

The goal of this paper is to analyse what is the effect of an asymmetric distribution of mass in the central parts of the galaxy on the external spiral structure. To introduce this asymmetry, we displace the bulge potential along the x -axis (main axis of the bar) towards the equilibrium point placed at the right end of the bar. The bulge centre is then located at $(x_d, 0, 0)$ using several values for the displacement x_d (in kpc), namely: (0,0,0), (0.5,0,0), (1,0,0) and (1.5,0,0). We move the centre of our potential model to the resulting centre of mass of the system. The plot of the equal density contours of the resulting models are shown in Fig. 3. Note that the displacement of the bulge along the main axis of the bar creates an asymmetry in the central part of the model and around the liberation points L_1 and L_2 .

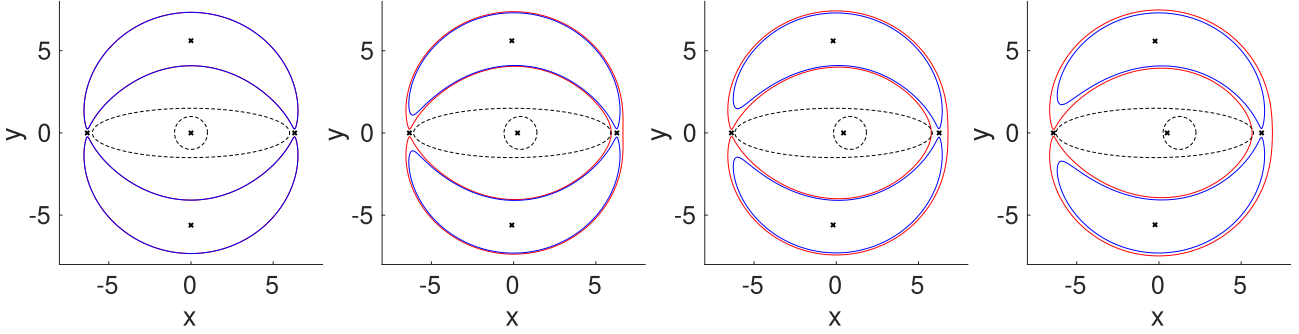


Figure 5. Zero velocity curves for a Jacobi constant slightly above to that of L_1 (blue) and for one slightly above to that of L_2 (red). Equilibrium points of the system are marked with a cross. The Ferrers bar and the Plummer bulge are outlined by dotted black curves. From left to right: Bulge centred at $(0,0,0)$, $(0.5,0,0)$, and $(1,0,0)$ and at $(1.5,0,0)$.

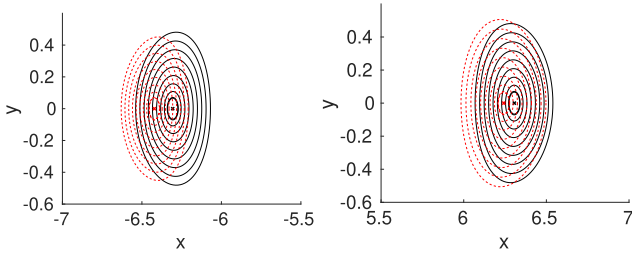


Figure 6. Lyapunov family of periodic orbits around L_i , $i = 1, 2$, for a range of values of the Jacobi constant in $(C_{J,L_i}, C_{J,L_i} + 10^{-4})$. Solid black line: (x, y) projection of the family around L_2 (left) and L_1 (right) for the symmetric model with bulge centred at $(0,0,0)$, $C_{J,L_i} = -0.2338$, $i = 1, 2$. Dotted red line: (x, y) projection of the family around L_2 (left) and L_1 (right) for the asymmetric model with bulge centred at $(1.5,0,0)$, $C_{J,L_2} = -0.2358$, $C_{J,L_1} = -0.2331$.

The rotation curves of the model, defined as $V_{\text{rot}}^2 = r \frac{d\phi}{dr}$, where the potential is $\phi = \phi_d + \phi_b + \phi_{bl}$ with the selected values of the parameters and for the above explained positions of the bulge displacement, are shown in Fig. 4. The resulting rotation curve is reasonably flat in the outer parts and displays only minor differences in the position of the maximum.

4 DYNAMICS OF THE MODELS

The solutions of $\nabla\phi_{\text{eff}} = 0$ in rotating coordinates give five Lagrangian equilibrium points of the model (L_i , $i = 1, \dots, 5$). Points L_1 and L_2 are linearly unstable points and lie on the x -axis at the ends of the bar. Point L_3 is linearly stable and is placed on the origin of coordinates in the case of a symmetric model. Points L_4 and L_5 are also linearly stable and located out of the x -axis. A detailed explanation of the dynamics around these points can be found in Athanassoula et al. (1983), Romero-Gómez et al. (2006), and Sánchez-Martín et al. (2016).

The regions where $\phi_{\text{eff}} > C_J$ are forbidden regions for a star of energy C_J . In the plane, these regions are delimited by the zero velocity curves, which are defined by the level surfaces $\phi_{\text{eff}} = C_J$ intersected with $z = 0$. In Fig. 5, we show the zero velocity curves corresponding to an energy slightly above that of the equilibrium point, $C_{J,L_i} + \delta$, for the models with off-centred bulges in Fig. 4, i.e. setting the values $x_d = 0, 0.5, 1, 1.5$. These zero velocity curves limit the inner and outer regions in the galaxy. In the symmetric case ($x_d = 0$), the energy of both equilibrium points L_1 and L_2 is the same,

$C_{J,L_1} = C_{J,L_2}$. For the asymmetric cases, as x_d grows C_{J,L_2} becomes smaller than C_{J,L_1} , which makes the zero velocity curves related to L_1 more open at the opposite point.

Particular attention is given in this work to the unstable points L_1 and L_2 . They are surrounded by planar and vertical families of Lyapunov periodic orbits, which are unstable in the neighbourhood of the equilibrium point. The relevant family for the transport of matter between the inner and outer regions of the galaxy is the planar family (Romero-Gómez et al. 2009). Fig. 6 shows the (x, y) projection of the planar family for the models with $x_d = 0$ (solid black line) and $x_d = 1.5$ (dotted red line). The family around L_2 is displayed at the left panel and that around L_1 at the right one. In the symmetric case ($x_d = 0$) both families coincide, whereas in the asymmetric one ($x_d = 1.5$) the family around L_2 is smaller than the one around L_1 .

These critical points are characterized by the superposition of a saddle and two harmonic oscillations in the rotating frame. Consequently, for a given Jacobi constant, stable and unstable invariant manifolds emanate from the periodic Lyapunov orbit around each point. The stable manifold is defined as the set of orbits that asymptotically tend to the periodic orbit forward in time and the unstable manifold consists of those orbits that depart asymptotically from the periodic orbit. These latter manifolds drive the escape orbits that are responsible for the visible trajectories, in the form of arms and rings. Fig. 7 shows the invariant manifolds associated with L_1 and L_2 for the set of models where $x_d = 0, 0.5, 1$, and 1.5 . The effect of an asymmetric mass distribution, modelled by the displacement of the bulge, makes the exterior manifold that emanates from L_2 to differ from the invariant manifold associated with L_1 .

The transit orbits trapped inside the manifolds are in charge of the transfer of matter, from the inner to the outer regions delimited by the zero velocity curves (Romero-Gómez et al. 2006; Gidea & Masdemont 2007; Sánchez-Martín, Masdemont & Romero-Gómez 2018). As the dynamics of our system (4) takes place in a four-dimensional phase space when we consider orbits with $z = \dot{z} = 0$ (the plane $z = 0$ is invariant), the intersection of the trajectories of the inner branch of the stable invariant manifold of a Lyapunov orbit with the hyperplane S defined by the section $x = 0$ in phase space gives a closed curve in the (y, \dot{y}) projection. Given a pair (y, \dot{y}) and an energy level, this lets us define a state on S by selecting $(0, y, 0, \dot{x}, \dot{y}, 0)$, where \dot{x} is determined by the fixed energy level of the Lyapunov orbit and the orientation of the crossing, taking into account equation (8),

$$\dot{x} = \sqrt{-\dot{y}^2 + \Omega^2 y^2 - 2\phi(0, y, 0) - (C_{J,L_i} + \delta)}, \quad (9)$$

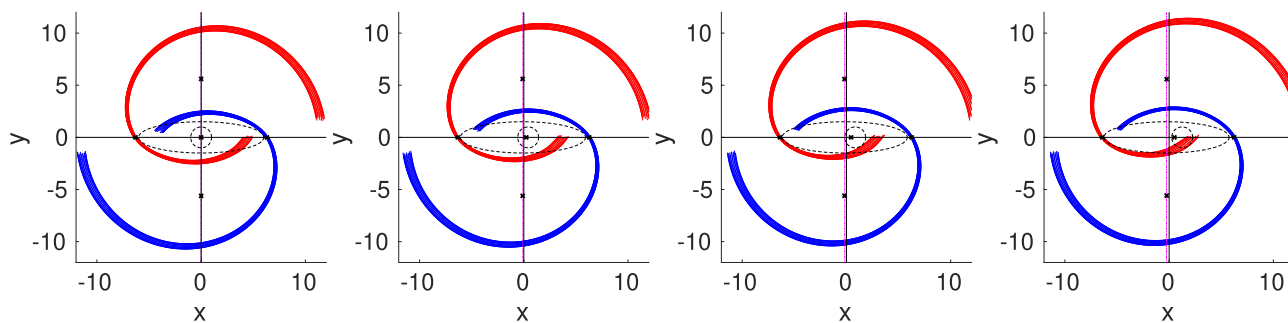


Figure 7. Unstable invariant manifolds associated with the Lyapunov periodic orbits of L_1 and L_2 . The position of the equilibrium points is marked with crosses. The bar and the bulge are outlined by dotted black curves. The reference system is marked with a solid black line and the centre of the bar with a dotted magenta line. From left to right: Bulge centred at $(0,0,0)$, $(0.5,0,0)$, and $(1,0,0)$ and at $(1.5,0,0)$.

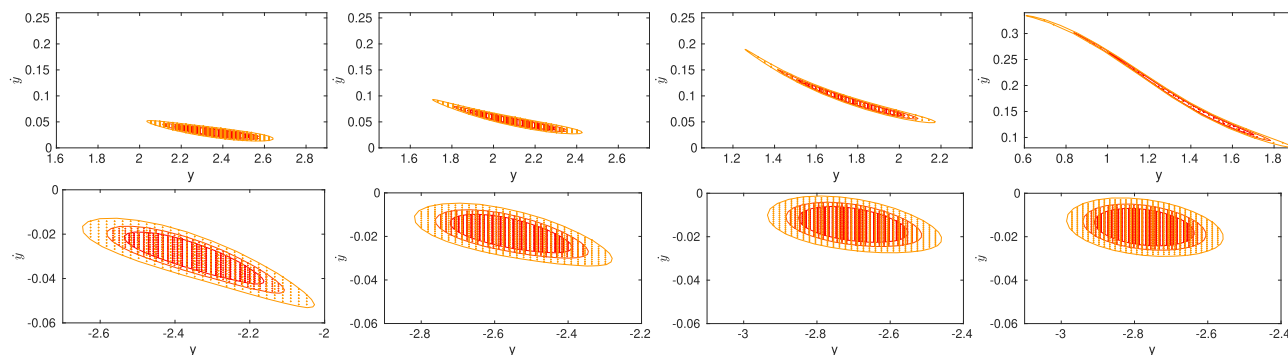


Figure 8. (y, \dot{y}) projection of the intersection of the plane S with the stable manifolds associated to three orbits with different Jacobi constant of the Lyapunov family around L_2 (top) and L_1 (bottom). The intersection of each manifold is in a colour, from red to yellow, according to the energy of the manifold. Initial conditions distributed inside each curve are marked with a cross with the same colour as the curve. From left to right: Bulge centred at $(0,0,0)$, $(0.5,0,0)$, $(1,0,0)$, and $(1.5,0,0)$. Note that the axis limits are different but their scale and range length are constant in each row.

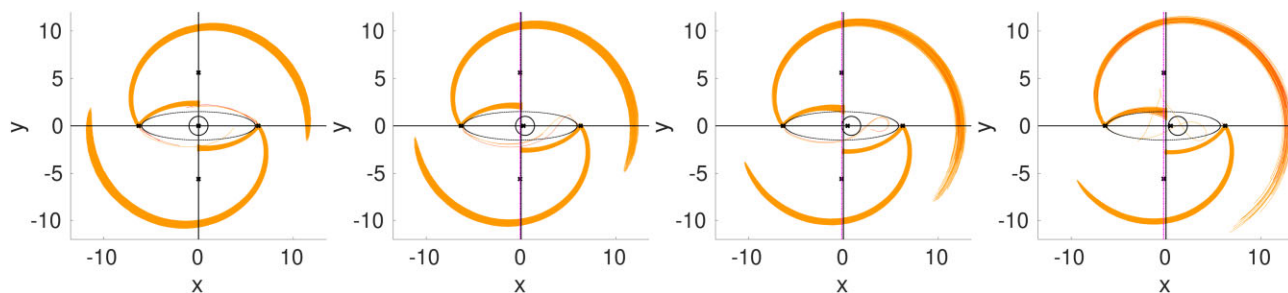


Figure 9. Orbits resulting from the integration of the initial conditions of Fig. 8. Equilibrium points marked in red. Bar and bulge outlined by dotted black curves. The reference system is marked with a solid black line and the centre of the bar with a dotted magenta line. From left to right: Bulge centered at $(0,0,0)$, $(0.5,0,0)$, and $(1,0,0)$ and at $(1.5,0,0)$.

with $C_{J,L_i} + \delta$ the energy of the Lyapunov orbit around the point L_i , $i = 1, 2$, slightly above that of the equilibrium point. The forward in time integration of initial conditions corresponding to (y, \dot{y}) points inside the closed curve establishes the trajectories of the particles confined inside the invariant manifold that transit from the inner to the outer region.

This procedure enables us to quantify the amount of matter transferred inside each invariant manifold associated with any energy level and, consequently, from each spiral arm of the galaxy. Fig. 8 represents the (y, \dot{y}) projection of the intersection with the hyperplane S of the invariant manifolds arising from three orbits

with different Jacobi constants in the Lyapunov family around L_2 (top), and the same corresponding orbits for L_1 (bottom). The three closed curves are displayed with different colours, from red to yellow, according to the increasing Jacobi constant. The initial conditions located inside each of the closed curves are marked with crosses of the same colour as the curve. From left to right, the figure displays the (y, \dot{y}) projection for the models with bulge centre ranging from $(0,0,0)$ to $(1.5,0,0)$. The main feature to notice in this figure is the narrowing and stretching of the curves as the bulge moves away from the L_2 equilibrium point. This constriction marks the difference between initial conditions for the escape orbits related with L_2 and

those related to L_1 . The initial conditions emanating from near L_2 are more extended along the y -axis, resulting in a dispersion in space of the orbits enclosed by the manifold. As we integrate forward in time these initial conditions, we obtain fewer escape orbits, and dispersed in a wider region, in comparison to those emanating near L_1 . So, the spiral arm defined by these orbits becomes more spread out and less bright. The result of these integrations is exhibited in Fig. 9 where it can be appreciated how the orbits inside the invariant manifolds develop the arms. The orbits corresponding to the L_1 point are more concentrated as the density of the bar increases in the region close to L_1 .

5 DISCUSSION AND CONCLUSIONS

The goal of this work is to analyse the relation between the asymmetric arms observed in certain barred galaxies and the mass distribution in the central part of the galaxy. We propose and show that there is a strong correlation between their asymmetries. The models used to study this fact consist of a superposition of a bar and an off-centred bulge. The displacements of the bulge along the main axis of the bar introduce an increasing asymmetry in the central part of the model. When the centre of mass of the galaxy is displaced along the major axis of the bar, the zero velocity curves of the effective potential become asymmetric: the one at the opposite side of the displacement becomes more open (see Fig. 5). We show that this asymmetry between the zero velocity curves in their opening is carried to the orbits trapped by invariant manifolds around the Lagrangian equilibrium points L_1 and L_2 . These orbits become asymmetric as well, with the arm at the opposite side of the displacement wider and more spread out. We quantify this effect by computing the fraction of orbits trapped by the manifolds. The procedure consists in intersecting the manifold with a hyperplane and, inside the resulting closed curve in the (y, \dot{y}) projection, obtaining the set of points with the same energy of the manifold as initial conditions that characterize the escaping orbits.

Indeed, the above closed curve turns out to be the most relevant feature in order to predict the asymmetry of the arms. When the bulge is displaced along the main axis of the bar, causing an asymmetry in the density distribution of the model, the closed curves around the equilibrium point at the end of the less dense side of the bar, narrow. This leads to a smaller measure of states in phase space that become initial conditions for escaping orbits. Moreover, these closed curves are more stretched, making the distribution of the points inside them more spread out in space. Both aspects are responsible for the resulting ragged and dispersed spiral arms in the less dense end of the bar, while the arm associated with the denser end becomes brighter and well defined.

The dynamics of off-centred bars have been studied using analytical models (Colin & Athanassoula 1989), showing how the Lagrangian points vary as a function of the displacement with respect to the centre of mass of the galaxy. Łokas (2021) digs into the barred galaxies in the IllustrisTNG simulations to check how common asymmetric and off-centred bars are and study its possible origin, concluding that asymmetric bars are persistent in time and this asymmetry may be due to the interaction with a companion galaxy or due to the disc itself being asymmetric. In either case, no further development has been proposed to link the asymmetry in the bar with the one-armed dominant spiral structure.

As shown in Fig. 1, this is a quite common phenomenon in barred galaxies. In particular, the dynamics of NGC 1300 have been studied in detail by Patsis et al. (2010), including an orbital analysis. The isocontours of a smooth K -band image (see their Fig. 1) show a

clear asymmetric bar distribution leading to an asymmetry in the spiral arms, which is reproduced by different orbital models. Other examples of one-armed dominated galaxies with an asymmetric bar may be as follows: NGC 4027 (Phookun et al. 1992), the density contours show an asymmetric and off-centred bar leading to a mass distribution dominated by an $m = 1$ mode, though a weak counterpart is also clear; the Large Magellanic Cloud (de Vaucouleurs & Freeman 1972), showing a rotational asymmetry, which is confirmed by more recent studies (e.g. Jiménez-Arranz et al. 2022; Niederhofer et al. 2022, and references therein).

To sum up, we show that asymmetric arms are a common feature in barred galaxies and that there is a clear correlation between arm asymmetry and the displacement of the centre of mass caused by an asymmetric central density distribution. Escaping orbits trapped in the invariant manifolds of an asymmetric bar distribution are asymmetric and the limiting case would be to have only one-armed barred spiral.

ACKNOWLEDGEMENTS

P.S.M. thanks the Spanish Ministry of Economy for grant numbers PID2020-117066GB-I00 and PID2021-123968NB-I00. J.J.M. thanks MINECO-FEDER for the grant number PID2021-123968NB-I00 and the Catalan government for grant number 2017SGR-1049. M.R.G. thanks the Spanish Ministry of Science for grant number MICIU/FEDER RTI2018-095076-B-C21, and the Institute of Cosmos Sciences University of Barcelona (ICCUB, Unidad de Excelencia ‘María de Maeztu’) for grant number CEX2019-000918-M.

Funding for the Sloan Digital Sky Survey IV has been provided by the Alfred P. Sloan Foundation, the U.S. Department of Energy Office of Science, and the Participating Institutions. SDSS (www.sdss.org) acknowledges support and resources from the Center for High-Performance Computing at the University of Utah.

DATA AVAILABILITY

The data underlying this article are available in the article.

REFERENCES

- Athanassoula E., Bienaymé O., Martinet L., Pfenniger D., 1983, *A&A*, 127, 349
- Bundy K. et al., 2015, *ApJ*, 798, 7
- Colin J., Athanassoula E., 1989, *A&A*, 214, 99
- Considère S., Athanassoula E., 1982, *A&A*, 111, 28
- de Vaucouleurs G., Freeman K. C., 1972, *Vistas Astron.*, 14, 163
- Ferrers N. M., 1877, *Q. J. Pure Appl. Math.*, 14, 1
- García-Gómez C., Barberà C., Athanassoula E., Bosma A., Whyte L., 2004, *A&A*, 421, 595
- García-Gómez C., Athanassoula E., Barberà C., Bosma A., 2017, *A&A*, 601, A132
- Gidea M., Masdemont J. J., 2007, *Int. J. Bifur. Chaos*, 17, 1151
- Iye M., Okamura S., Hamabe M., Watanabe M., 1982, *ApJ*, 256, 103
- Jiménez-Arranz Ó. et al., 2022, *A&A*, 669, A91, preprint ([arXiv:2210.01728](https://arxiv.org/abs/2210.01728))
- Lee Y. H., Ann H. B., Park M. G., 2019, *ApJ*, 872, 97
- Łokas E. L., 2021, *A&A*, 655, A97
- Miyamoto M., Nagai R., 1975, *PASJ*, 27, 533
- Niederhofer F. et al., 2022, *MNRAS*, 512, 5423
- Patsis P. A., Kalapotharakos C., Grosbol P., 2010, *MNRAS*, 408, 22
- Pfenniger D., 1984, *A&A*, 134, 373
- Phookun B., Mundy L. G., Teuben P. J., Wainscoat R. J., 1992, *ApJ*, 400, 516
- Plummer H. C., 1911, *MNRAS*, 71, 460

- Romero-Gómez M., Masdemont J. J., Athanassoula E., García-Gómez C., 2006, *A&A*, 453, 39
- Romero-Gómez M., Masdemont J. J., García-Gómez C., Athanassoula E., 2009, *CNSNS*, 14, 4123
- Sánchez-Martín P., Romero-Gómez M., Masdemont J. J., 2016, *A&A*, 588, A76
- Sánchez-Martín P., Masdemont J. J., Romero-Gómez M., 2018, *A&A*, 618, A72
- Skokos Ch., Patsis P. A., Athanassoula E., 2002, *MNRAS*, 333, 847
- Tonini C., Mutch S. J., Croton D. J., Wyithe J. S. B., 2016, *MNRAS*, 459, 4109

This paper has been typeset from a $\text{\TeX}/\text{\LaTeX}$ file prepared by the author.